Mon. Not. R. Astron. Soc. **370,** 1309–1323 (2006) doi:10.1111/j.1365-2966.2006.10552.x

Detecting Sunyaev–Zel'dovich clusters with *Planck* – I. Construction of all-sky thermal and kinetic SZ maps

B. M. Schäfer,[1⋆] C. Pfrommer,[1⋆] M. Bartelmann,[2⋆] V. Springel[1⋆] and L. Hernquist[3⋆]

[1]*Max-Planck-Institut für Astrophysik, Karl-Schwarzschild-Straße 1, Postfach 1317, 85741 Garching, Germany*
[2]*Institut für theoretische Astrophysik, Universität Heidelberg, Albert-Ueberle-Straße 2, 69120 Heidelberg, Germany*
[3]*Harvard-Smithsonian Center for Astrophysics, 60 Garden Street, Cambridge, MA 02138, USA*

Accepted 2006 May 10. Received 2006 March 3; in original form 2004 July 5

ABSTRACT

All-sky thermal and kinetic Sunyaev–Zel'dovich (SZ) maps are presented for assessing how well the *Planck* mission can find and characterize clusters of galaxies, especially in the presence of primary anisotropies of the cosmic microwave background (CMB) and various Galactic and ecliptic foregrounds. The maps have been constructed from numerical simulations of structure formation in a standard Λ cold dark matter (ΛCDM) cosmology and contain all clusters out to redshifts of $z = 1.46$ with masses exceeding $5 \times 10^{13}\,\mathrm{M}_\odot\,\mathrm{h}^{-1}$. By construction, the maps properly account for the evolution of cosmic structure, the halo–halo correlation function, the evolving mass function, halo substructure and adiabatic gas physics. The velocities in the kinetic map correspond to the actual density environment at the cluster positions. We characterize the SZ-cluster sample by measuring the distribution of angular sizes, the integrated thermal and kinetic Comptonizations, the source counts in the three relevant *Planck* channels, and give the angular power spectra of the SZ sky. While our results are broadly consistent with simple estimates based on scaling relations and spherically symmetric cluster models, some significant differences are seen which may affect the number of cluster detectable by *Planck*.

Key words: methods: numerical – galaxies: clusters: general – cosmic microwave background.

1 INTRODUCTION

The Sunyaev–Zel'dovich (SZ) effects (Sunyaev & Zel'dovich 1972, 1980; Rephaeli 1995; Birkinshaw 1999) have evolved from physical peculiarities to valuable and sound observational tools in cosmology. The thermal SZ effect arises because photons of the cosmic microwave background (CMB) experience Compton collisions with electrons of the hot plasma inside clusters of galaxies and are spectrally redistributed. The amplitude of the modulation of the Planckian CMB spectrum is a measure of the cluster electron column density and temperature. Alternatively, CMB photons may gain energy by elastic Compton collisions with electrons of the intra-cluster medium (ICM) due to the peculiar motion of the cluster relative to the CMB. This so-called kinetic SZ effect is proportional to the peculiar velocity weighted electron column density and directly measures the cluster's velocity component parallel to the line-of-sight relative to the comoving CMB frame.

The advancement in sensitivity and angular resolution of submillimetre and microwave receivers has allowed high-quality interferometric imaging of more than 50 clusters of galaxies by ground-based telescopes (Carlstrom, Holder & Reese 2002) out to redshifts of $\sim$0.8, despite incomplete coverage of the Fourier plane. Apart from its primary scientific objective, namely the cartography of the CMB with angular resolutions close to 5 arcmin, the upcoming *Planck* mission (Mandolesi et al. 1995; Tauber 2001) will be a unique tool for observing clusters of galaxies by their SZ signature. *Planck* is expected to yield a cluster catalogue that will surpass the classic optical Abell catalogues or any existing X-ray catalogue in numbers as well as in depth and sky coverage.

The capability of *Planck* to detect SZ clusters has been the subject of many recent works, pursuing analytical (Aghanim et al. 1997; Bartelmann 2001; Delabrouille, Melin & Bartlett 2002; Moscardini et al. 2002), semi-analytical (Kay, Liddle & Thomas 2001; Hobson & McLachlan 2003) and numerical approaches (Herranz et al. 2002; White 2003). Their consensus is an expected total number of a few times 10^4 clusters and the detectability of (sufficiently massive) clusters out to redshifts of $z \lesssim 1$. The authors differ mainly in the expected distribution of the detectable clusters in redshift z. Where addressed, the authors remain sceptic about the detectability of the kinetic SZ effect.

As a result of various approximations made, there are limitations in these studies. Concerning the SZ profiles of isolated clusters, simplifying assumptions like spherical symmetry, complete

⋆E-mail: spirou@mpa-garching.mpg.de (BMS); pfrommer@mpa-garching.mpg.de (CP); mbartelmann@ita.uni-heidelberg.de (MB); volker@mpa-garching.mpg.de (VS); lars@cfa.harvard.edu (LH)

ionization and isothermality have usually been made. Analytical treatments mostly rely on β-profiles for modelling the spatial variation of the Compton-y parameter. Temperature models mostly make use of scaling laws derived from spherical collapse theory or are taken from X-ray observations. Naturally, the halo–halo correlation function is not taken account of, neither do the velocities correspond to the actual density environment; they are commonly drawn from a (Gaussian) velocity distribution.

The primary application of the all-sky SZ maps would lie in the assessment of the extent to which cluster substructure and deviations from spherical symmetry, the halo–halo clustering and deviations from the scaling laws alter the predictions made for *Planck* based on analytic methods. Further complications include Galactic foregrounds (for a comprehensive review of foregrounds concerning *Planck*, see Bouchet & Gispert 1999), the thermal emission from planets and minor celestial bodies of the solar system, beam patterns and spatially non-uniform instrumental noise. For investigating this issue, realistic all-sky maps of the thermal and kinetic SZ effects are essential.

In our map construction, we take advantage of two numerical simulations of cosmic structure formation: the Hubble-volume simulation that provided a well-sampled cluster catalogue covering a large volume and, secondly, a set of template clusters resulting from a gas-dynamical simulation on much smaller scales, allowing us to extract template clusters. For all clusters of the Hubble-volume simulation, a suitable template was chosen, and after having performed a scaling operation to improve the match, it is projected on to the celestial sphere at the position requested by the Hubble-volume catalogue. By construction, the resulting all-sky SZ maps show halo–halo correlation even on large angular scales, incorporate the evolution of the mass function and have the correct size distribution. In the kinetic SZ map, it is ensured that the cluster peculiar velocities correspond to the ambient cosmological density field. Furthermore, the template clusters do exhibit realistic levels of substructure and departures from isothermality, and their ensemble properties also account for scatter around the idealized scaling laws. Therefore, most of the imperfections of traditional approaches will be remedied by our map construction process.

However, there are impediments that could not be disposed of. They include gas physics beyond adiabaticity, e.g. radiative cooling and supernova feedback, that significantly alter the baryon distribution and temperature profiles of the ICM and hence the SZ amplitude, incomplete ionization, inclusion of filamentary structures and uncollapsed objects or diffuse gas. Another process influencing the thermal history of the ICM is reionization, which also had to be excluded. Yet another complication is non-thermal particle populations in clusters of galaxies that give rise to the relativistic SZ effect (Wright 1979; Enßlin & Kaiser 2000). An approach similar to ours has been pursued by Geisbüsch, Kneissl & Hobson (2005), who placed spherically symmetric β-profiles for describing the thermal Comptonization at the positions given by the Hubble-volume simulation.

This paper is structured as follows. After the definition of the basic SZ quantities in Section 2, the simulations are outlined in Section 3. The construction of the maps is described in detail in Section 4 and the properties of the resulting maps are compiled in Section 5. Finally, the conclusions are presented in Section 6.

2 SZ DEFINITIONS

The thermal and kinetic SZ effects are the most important sources of secondary anisotropies in the CMB. Compton interactions of CMB photons with electrons of the ionized ICM give rise to these effects and induce surface brightness fluctuations in the CMB sky, either because of the thermal motion of the ICM electrons (thermal SZ) or because of the bulk motion of the cluster itself (kinetic SZ).

The relative change $\Delta T/T$ in thermodynamic CMB temperature at position $\boldsymbol{\theta}$ as a function of dimensionless frequency $x = h\nu/(k_\mathrm{B}\,T_\mathrm{CMB})$ due to the thermal SZ effect is given by equation (1):

$$\frac{\Delta T}{T}(\boldsymbol{\theta}) = y(\boldsymbol{\theta})\left(x\frac{\mathrm{e}^x+1}{\mathrm{e}^x-1}-4\right) \text{ with} \tag{1}$$

$$y(\boldsymbol{\theta}) = \frac{\sigma_\mathrm{T}k_\mathrm{B}}{m_\mathrm{e}c^2}\int \mathrm{d}l\; n_\mathrm{e}(\boldsymbol{\theta},l)T_\mathrm{e}(\boldsymbol{\theta},l), \tag{2}$$

where the amplitude y of the thermal SZ effect is commonly known as the thermal Comptonization parameter. It is proportional to the line-of-sight integral of the temperature weighted thermal electron density (cf. equation 2). $m_\mathrm{e}, c, k_\mathrm{B}$ and σ_T denote electron mass, speed of light, Boltzmann's constant and the Thompson cross-section, respectively. The kinetic SZ effect arises due to the motion of the cluster relative to the CMB rest frame parallel to the line-of-sight. The respective temperature change is given by

$$\frac{\Delta T}{T}(\boldsymbol{\theta}) = -w(\boldsymbol{\theta}) \text{ with } w(\boldsymbol{\theta}) = \frac{\sigma_\mathrm{T}}{c}\int \mathrm{d}l\; n_\mathrm{e}(\boldsymbol{\theta},\boldsymbol{l})\upsilon_\mathrm{r}(\boldsymbol{\theta},l). \tag{3}$$

Here, υ_r is the radial component of the cluster velocity, i.e. the velocity component parallel to the line-of-sight. The convention is such that the CMB temperature is increased, if the cluster is moving towards the observer, i.e. if $\upsilon_\mathrm{r} < 0$. In analogy to y, the quantity w is referred to as the kinetic Comptonization parameter.

3 SIMULATIONS

Due to the SZ clusters being detectable out to very large redshifts, their clustering properties on very large angular scales and the requirement of reducing cosmic variance when simulating all-sky observations as will be performed by *Planck*, there is the need for very large simulation boxes, encompassing look-back distances to redshifts of the order of $z \simeq 1$ which corresponds to comoving scales exceeding 2 Gpc. Unfortunately, a simulation incorporating dark matter and gas dynamics that covers cosmological scales of that size down to cluster scales and possibly resolving cluster substructure is presently beyond computational feasibility.

For that reason, a hybrid approach is pursued by combining results from two simulations: the Hubble-volume simulation (Colberg et al. 2000; Jenkins et al. 2001), and a smaller scale simulation including (adiabatic) gas physics (White, Hernquist & Springel 2002). The analysis undertaken by Bartelmann (2001) gives expected mass and redshift ranges for detectable thermal SZ clusters, which are covered completely by the all-sky SZ map presented here.

The assumed cosmological model is the standard ΛCDM cosmology, which has recently been supported by observations of the *Wilkinson Microwave Anisotropy Probe* (*WMAP*) satellite (Spergel et al. 2003). Parameter values have been chosen as $\Omega_\mathrm{M} = 0.3$, $\Omega_\Lambda = 0.7$, $H_0 = 100\,h\,\mathrm{km\,s^{-1}\,Mpc^{-1}}$ with $h = 0.7$, $\Omega_\mathrm{B} = 0.04$, $n_\mathrm{s} = 1$ and $\sigma_8 = 0.9$.

3.1 Hubble-volume simulation

The Hubble-volume simulation is one of the largest simulations of cosmic structure formation carried out to date. The simulation domain is a box of comoving side length $3\,\mathrm{Gpc\,h^{-1}}$ (for the standard ΛCDM cosmology) and comprises 10^9 dark matter particles.

Table 1. Basic characteristics of the light-cone outputs used for compiling a cluster catalogue. The columns denote the label of the data set, the range in redshift z, the solid angle Ω covered, the number of objects $N_{\rm halo}$ retrieved and the geometrical shape.

Data set	z range	Ω/sr	$N_{\rm halo}$	Shape
MS	$0.0 \leqslant z \leqslant 0.58$	4π	564 818	Sphere
NO	$0.58 < z \leqslant 1.46$	$\pi/2$	182 551	Northern octant shell
PO	$0.58 < z \leqslant 1.46$	$\pi/2$	185 209	Southern octant shell

The simulations used were carried out by the Virgo Supercomputing Consortium using computers based at the Computing Centre of the Max-Planck Society in Garching and at the Edinburgh Parallel Computing Centre. The data are publicly available for download.[1]

The light-cone output of the Hubble-volume simulation (Evrard et al. 2002) was used for compiling a cluster catalogue. This ensures that the abundance of clusters at any given redshift z corresponds to the level of advancement in structure formation up to this cosmic epoch. The minimal mass was set to $5 \times 10^{13}\,{\rm M}_\odot\,{\rm h}^{-1}$, which roughly corresponds to the transition mass between a rich group of galaxies and a cluster. In order to cover redshifts out to the anticipated limit for *Planck*, light-cone outputs of differing geometry were combined: first, a sphere covering the full solid angle of 4π was used for redshift radii of $z = 0$–0.58. For redshifts exceeding $z = 0.58$, the northern and southern octant data sets were added. The octant data sets span a solid angle of $\pi/2$ and were replicated by rotation in order to cover the full sphere. Table 1 summarizes the properties of the different output geometries. In this way, a cluster catalogue with cluster mass M, position on the sky $\boldsymbol{\theta}$, redshift z and peculiar velocity $\upsilon_{\rm r}$ projected on to the line-of-sight was compiled, comprising a total number of 2 035 858 clusters. For the sky-map construction, the positions $\boldsymbol{\theta}$ were interpreted as ecliptic coordinates, the default coordinate system for *Planck*.

Here, it should be mentioned that the combination of different outputs gives rise to boundary discontinuities, at the surface of the central sphere as well as on the faces of the octant shells. These discontinuities not only show up in the spatial halo distribution, but also show up in the velocities of clusters close to simulation box boundaries. Furthermore, the cluster catalogues exhibit small completeness deficiencies close to the edges of the simulation domain.

The Hubble-volume simulation is ideally suited for the construction of a SZ all-sky map because the population of clusters observable with *Planck* and most interesting for the estimation of cosmological parameters will consist of massive systems situated at intermediate redshifts. Bartelmann (2001) investigated detection criteria for SZ observations with *Planck* and derived a delimiting line in the M–z-plane. Given this analytic estimate, the Hubble-volume simulation provides a sufficient population of target clusters as it extends to objects well below the anticipated detection limit. For the investigation of low-mass close-by systems, we provide SZ maps to fit to SZ maps derived from a constrained realization of the local Universe constructed by Dolag et al. (2005). It should be noted, however, that the fluctuating SZ background is only partially reproduced due to the lack of low-mass objects. This incompleteness is discussed in detail in Sections 4.4 and 5.5.

3.2 Small-scale SPH cluster simulations

A hydrodynamical simulation of cosmological structure formation (White et al. 2002) constitutes the basis of the SZ-template map construction. The simulation was performed with the GADGET code[2] (Springel, Yoshida & White 2001) using the 'entropy-conserving' formulation of smoothed particle hydrodynamics (SPH) (Springel & Hernquist 2002). The simulation, first analysed in White et al. (2002), followed 216^3 dark matter particles as well as 216^3 gas particles in a cubical box of comoving side length $100\,{\rm Mpc\,h}^{-1}$ with periodic boundary conditions. Purely adiabatic gas physics and shock heating were included, but radiative cooling and star formation were ignored, which, however, does not result in significant differences in SZ morphology, as shown by White et al. (2002), but would impact on the scaling relations as demonstrated by da Silva et al. (2001). We analyse 30 output redshifts ranging from $z = 0$ to 1.458. The comoving spacing along the line-of-sight of two subsequent outputs is $100\,{\rm Mpc\,h}^{-1}$. Haloes were identified using a friends-of-friends algorithm with linking length $b = 0.164$, which yields all member particles of cluster-sized groups. We then employed a spherical overdensity code to estimate the virial mass and radius of each cluster.

We computed the mass $M_{\rm vir}$ inside a sphere of radius $r_{\rm vir}$, interior to which the average density was 200 times the critical density $\rho_{\rm crit} = 3H(z)^2/(8\pi G)$. This definition of the mass has been adopted to match the definition used by Evrard et al. (2002) in compiling the light-cone catalogue. Furthermore, this definition ensures the comparability of halo masses in different cosmologies. In the extraction of clusters from the hydrodynamic simulation, we imposed a lower mass threshold of $M_{\rm vir} \geqslant 5 \times 10^{13}\,{\rm M}_\odot\,{\rm h}^{-1}$ in order to match the lower mass limit adopted for the Hubble-volume cluster catalogue.

4 SZ MAP CONSTRUCTION

The construction of the all-sky SZ map proceeds in three steps: first, a set of template cluster maps is derived based on cluster data from a gas-dynamical simulation (Section 4.1). Then, for each of the clusters in the cluster catalogue obtained from the Hubble-volume simulation, a suitable hydrodynamical cluster template is selected, scaled in mass and temperature in order to better fit the cluster from the Hubble-volume catalogue (Section 4.2), and, for the kinetic sky map, boosted to the radial peculiar velocity required by the Hubble-volume simulation. The last step is the projection on to a spherical celestial map (Section 4.3). In the subsequent paragraph (Section 4.4), the completeness of the resulting SZ maps is investigated analytically.

4.1 SZ-template map preparation

Square maps of the Compton-y parameter of the selected clusters were generated by SPH projection of all friends-of-friends identified member gas particles on to a Cartesian grid with 128^2 mesh points. The (comoving) side length s of the map was adapted to the cluster size, such that the comoving resolution $g = s/128$ of the grid is specific to a given map.

If the particle p at position $\boldsymbol{r}_p = (x_p, y_p, z_p)$ has a smoothing length h_p, a SPH electron number density n_p and a SPH electron temperature T_p, the Compton-y parameter for the pixel at position

[1] http://www.mpagarching.mpg.de/galform/virgo/hubble

[2] http://www.mpagarching.mpg.de/galform/gadget/index.shtml

$\boldsymbol{x}$ is given by

$$y(\boldsymbol{x}) = \frac{\sigma_\mathrm{T} k_\mathrm{B}}{m_\mathrm{e} c^2} \frac{h_p^3}{g^2} \sum_p \left[\int_{x-g/2}^{x+g/2} \mathrm{d}x_p \times \int_{y-g/2}^{y+g/2} \mathrm{d}y_p \int_{-h_p}^{h_p} \mathrm{d}z_p \, \mathcal{K}\left(\frac{r}{h_p}\right) n_p T_p \right] \quad (4)$$

$$\text{with } r = \sqrt{(x_p - x)^2 + (y_p - y)^2 + z_p^2}. \quad (5)$$

Here, we assume complete ionization and primordial element composition of the ICM for the determination of electron number density and temperature. In this way, we produce projections along each of the three coordinate axes. The function $\mathcal{K}$ is the spherically symmetric cubic spline kernel suggested by Monaghan & Lattanzio (1985), which was also used in the SPH simulation:

$$\mathcal{K}(u) = \frac{8}{\pi} \times \begin{cases} 1 - 6u^2 + 6u^3, & 0 \leqslant u \leqslant 1/2 \\ 2(1-u)^3, & 1/2 < u \leqslant 1 \\ 0, & u > 1 \end{cases} \quad \text{with } u = r/h_p. \quad (6)$$

The fact that the kernel $\mathcal{K}$ has a compact support $u \in [0 \ldots 1]$ greatly reduces the computational effort.

The kinetic maps were treated in complete analogy: maps of the Thomson optical depth τ were derived by means of equation (7):

$$\tau(\boldsymbol{x}) = \sigma_\mathrm{T} \frac{h_p^3}{g^2} \sum_p \left[\int_{x-g/2}^{x+g/2} \mathrm{d}x_p \times \int_{y-g/2}^{y+g/2} \mathrm{d}y_p \int_{-h_p}^{h_p} \mathrm{d}z_p \, \mathcal{K}\left(\frac{r}{h_p}\right) n_p \right]. \quad (7)$$

In equation (7), the influence of velocity differences inside the clusters was omitted. At the stage of projecting the template clusters on to the spherical map, the τ-map obtained is boosted with the peculiar line-of-sight velocity v_r in units of the speed of light c required by the entry in the Hubble-volume catalogue in order to yield a Compton-w amplitude.

Neglecting velocity differences inside the clusters does not seriously affect the measurement of cluster peculiar velocities with the kinetic SZ effect as shown by Nagai, Kravtsov & Kosowsky (2003) and Holder (2004). Although internal velocities are comparable to the peculiar velocity of the cluster itself, averaging over a region defined by the virial radius reduces the scatter to less than $50\,\mathrm{km\,s^{-1}}$ which is small compared to the mean squared value for the peculiar velocity of $\sim 320\,\mathrm{km\,s^{-1}}$ found in the Hubble volume. Nagai et al. (2003) further report that this velocity average is an unbiased estimator of the actual radial velocity. The comparatively large beam of *Planck* with a width of 5.0 arcmin in the highest resolution channels will average the kinetic SZ amplitude over the cluster area for a large number of clusters such that the scatter in the measurement of the kinetic SZ amplitude will be small, even more so if the amount of substructure of a cluster can be modelled on the basis of a high-resolution X-ray map. A further point to note is the fact that the estimation of the kinetic SZ amplitude is not straightforward in the presence of the dominating thermal SZ effect (cf. Herranz et al. 2005).

In this way, a sample of 1518 individual template clusters was obtained, and maps for projections along all three coordinate axes were derived, yielding a total of 4554 template maps for each of the two SZ effects. Fig. 1 shows the distribution of clusters in the mass–redshift plane. Especially at high masses, the smooth growth of clusters by accretion can be clearly seen. Sudden jumps to larger masses are caused by the merging of low-mass clusters.

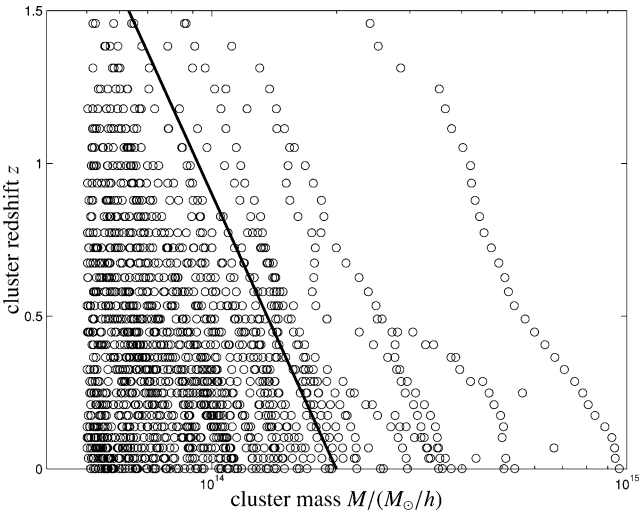

Figure 1. The population of our template clusters in the mass–redshift plane. The line separates the sparsely sampled region from the region in which a sufficient number of template clusters are available.

A limitation to our SZ map construction is immediately apparent: the 4554 cluster template maps derived from the hydrosimulation are not strictly independent, but merely show the same clusters at different redshift. Thus, the morphological variety remains limited, even though there is, of course, some variation in morphology due to accretion and merging events. This, however, may not be a severe restriction, keeping the wide *Planck* beams in mind, that are unlikely to resolve cluster substructure for a large fraction of detectable clusters. In this case, the simulation will pick up mismatches in Comptonization relative to the value expected from the spherical collapse model in conjunction with the Press–Schechter distribution of halo masses.

4.2 Cluster selection and scaling relations

In order to select a template map for projection, the closest template cluster in the $\log(M)$–z-plane for a given cluster from the Hubble-volume simulation was chosen. For the sparsely sampled region of the M–z-plane to the right of the line in Fig. 1, a cluster from a pool containing the most massive clusters to the right of this line in the redshift bin under consideration was drawn.

The template clusters are scaled in mass, temperature and spatial extent in order to yield a better match to the cluster from the Hubble-volume simulation according to formulae (8)–(10). The scaling is parametrized by the masses of the cluster of the Hubble-volume simulation $M_\mathrm{vir}^\mathrm{(Hubble)}$ and the template cluster $M_\mathrm{vir}^\mathrm{(template)}$:

$$q_M = \frac{M_\mathrm{vir}^\mathrm{(Hubble)}}{M_\mathrm{vir}^\mathrm{(template)}} \quad (8)$$

$$q_R = \frac{r_1 \left(M_\mathrm{vir}^\mathrm{(Hubble)}\right)^{r_2} + r_3}{r_\mathrm{vir}^\mathrm{(template)}} \quad (9)$$

$$q_\mathrm{T} = \frac{t_1 \left(M_\mathrm{vir}^\mathrm{(Hubble)}\right)^{t_2} + t_3}{t_1 \left(M_\mathrm{vir}^\mathrm{(template)}\right)^{t_2} + t_3}. \quad (10)$$

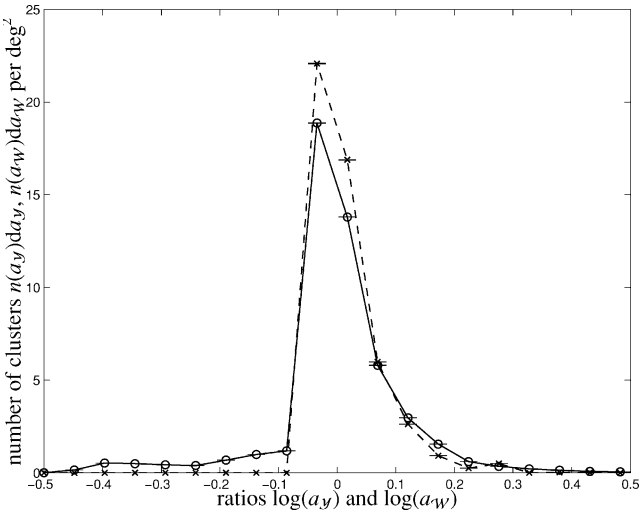

Figure 2. Distribution of the ratios $a_\mathcal{Y}$ (circles, solid line) and $a_\mathcal{W}$ (crosses, dashed line) that describes the impact of the mismatch between friends-of-friends masses and virial masses on the Comptonizations $\mathcal{Y}$ and $\mathcal{W}$.

The parameters r_i and t_i, $i \in \{1, 2, 3\}$, describing the scaling in size q_R and in temperature q_T were derived from template data: fits to the virial radius as a function of mass and of the mean temperature inside the virial sphere as a function of mass were applied to the data of simulation outputs binned in five data sets. This approach leaves the map construction independent of idealized assumptions, like the prediction of cluster temperatures from the spherical collapse model, or from electron temperature measurements deduced from X-ray observations and keeps the weak trend of cluster temperature with redshift z as contained in the simulations.

Although the scaling has been constructed in order to yield the best possible match between the template cluster and the target cluster from the Hubble-volume simulation, there are artefacts in irregular systems due to inconsistencies in cluster masses $M_\mathrm{fof}^\mathrm{(template)}$ determined with a friends-of-friends algorithm for identifying cluster member particles and the virial mass estimates $M_\mathrm{vir}^\mathrm{(template)}$ following from applying the spherical overdensity code. After the scaling, these mismatches may be expressed as

$$a_\mathcal{Y} = q_M q_\mathrm{T} M_\mathrm{fof}^\mathrm{(template)} \Big/ M_\mathrm{vir}^\mathrm{(Hubble)} \quad \text{and} \tag{11}$$

$$a_\mathcal{W} = q_M M_\mathrm{fof}^\mathrm{(template)} \Big/ M_\mathrm{vir}^\mathrm{(Hubble)}. \tag{12}$$

Fig. 2 shows the distribution of ratios $a_\mathcal{Y}$ and $a_\mathcal{W}$ for the entire Hubble-volume catalogue. Clearly, one recognizes large tails towards high values because clusters have, on average, to be scaled to higher masses. This is due to the fact that the hydrosimulation outlined in Section 3.2 does not sample the high-mass end of the Press–Schechter function satisfactorily, simply because of its small volume. Nevertheless, the mean of the distributions is close to one, which implies that the mismatches average out for the bulk of clusters.

4.3 Projection on to the celestial sphere

For storing all-sky maps, the HEALPIX[3] tesselation of the sphere proposed by Górski et al. (2005) has been chosen. In order to support structures as small as clusters, the N_side parameter has been set to 2048, resulting in a total number of $12\,N_\mathrm{side}^2 = 50\,331\,648$ pixels. The side length of one pixel is then approximately 1.71 arcmin, which is well below the anticipated *Planck* beam size of 5.0 arcmin in the highest frequency channels.

The scaled cluster maps are projected on to the spherical map by means of stereographic projection at the south ecliptic pole of the celestial sphere. By dividing the (comoving) position vector (x, y) of a given pixel on the template map by the comoving angular diameter distance $\chi(z)$ at redshift z, one obtains the coordinates (α, β) on the tangential plane. Then, the stereographic projection formulae yield the (Cartesian) position vector (ξ, η, ζ) of this point projected on to the unit sphere:

$$\boldsymbol{r} = (\xi, \eta, \zeta + 1) = \left(\frac{4\alpha}{4 + \alpha^2 + \beta^2}, \frac{4\beta}{4 + \alpha^2 + \beta^2}, \frac{\alpha^2 + \beta^2}{4 + \alpha^2 + \beta^2} \right). \tag{13}$$

In order to assign a Comptonization amplitude to a given HEALPIX pixel in the projection process, a solid angle weighted average is performed. For close-by clusters, the mesh size of the templates converted to angular units is larger than the HEALPIX pixel scale. For those clusters, the map is refined iteratively by subdivision of a pixel into four smaller pixels subtending a quarter of the original solid angle until the pixel size is well below the HEALPIX pixel scale. Before projection, the template maps are smoothed with a Gaussian kernel with $\Delta\theta = 2.0$ arcmin, which is comparable to the HEALPIX pixel scale. In this way, the destruction of structures is avoided by the combination of multiple template map pixels into a single HEALPIX pixel. This convolution does not affect the later usage for simulations concerning *Planck*: a second successive convolution with the narrowest beam results in an effective smoothing of 5.38 arcmin, which corresponds to a decrease in angular resolution of roughly 7.5 per cent.

Additionally, a rotation of the template map around the $\boldsymbol{e}_z$-axis about a random angle is performed in order to avoid spurious alignments of clusters. The projected pixels are then transported by Euler rotations of the vector (ξ, η, ζ) to the position requested by the Hubble catalogue.

4.4 Completeness of the all-sky SZ maps

The angular resolution of *Planck* will not allow to spatially resolve low-mass and high-redshift clusters. There will be a Compton-y background $\langle y_\mathrm{rbg} \rangle_\theta$ due to the higher number density of low-mass clusters compared to high-mass clusters which overcompensates their lower individual SZ signature. Since ideally any isotropic background could be removed, we only have to take into account the average background fluctuation level $\langle y_\mathrm{bg}^2 \rangle_\theta$ which is described by power spectrum statistics.

This section studies the influence of the background of unresolved SZ clusters in our all-sky map of SZ clusters on power spectrum statistics. Our simulation neglects the SZ signal of clusters both with masses smaller than $5 \times 10^{13}\,\mathrm{M}_\odot\,\mathrm{h}^{-1}$ and with redshifts $z > 1.5$. In principle, these missing clusters could be accounted for by drawing them from a particular realization of a *Poissonian random field* such that they obey the correct relative phase correlations, i.e. that they exhibit the observed local clustering properties.

However, there are large uncertainties about the baryon fraction $f_\mathrm{B} = \Omega_\mathrm{B}/\Omega_\mathrm{M}$ of low-mass haloes ($M_\mathrm{halo} < 5 \times 10^{13}\,\mathrm{M}_\odot\,\mathrm{h}^{-1}$) especially at higher redshifts. Analyses of X-ray observations of 45 local clusters ($z < 0.18$, only four of them lie at $z > 0.1$) carried out by Mohr, Mathiesen & Evrard (1999) and Arnaud & Evrard

[3]http://www.eso.org/science/healpix/

(1999) suggest a weak trend of the cluster baryon fraction f_B with cluster mass M and a deviation from the universal value, which may be due to feedback processes like galactic winds that more effectively deplete the ICM of baryons in low-mass compared to high-mass clusters. The behaviour of f_B at high redshifts is very uncertain, among other reasons because the relative importance of the different feedback processes at high redshift is yet unknown. This uncertainty is also reflected in different cooling rates and mechanisms, governing the ionization fraction of the electrons and the resulting SZ flux of a particular cluster. In the following, we study the contribution to the SZ flux of clusters with both masses smaller than $5 \times 10^{13}\,\mathrm{M}_\odot\,\mathrm{h}^{-1}$ and redshifts $z > 1.5$. Although the impact of this cluster population to the $\langle y_\mathrm{bg}\rangle$-statistics amounts to a significant fraction, this population has a negligible contribution to the more relevant $\langle y_\mathrm{bg}^2\rangle$-statistics which will be shown in the following. The unresolved cluster population is assumed to follow scaling relations derived from the spherical collapse model. Temperature T and halo mass M are assumed to be related by

$$\frac{k_\mathrm{B}T}{6.03\,\mathrm{keV}} = \left(\frac{M}{10^{15}\,\mathrm{M}_\odot\,\mathrm{h}^{-1}}\right)^{2/3} (1+z) \left[\frac{\Omega_0}{\Omega(z)}\right]^{1/3} \left[\frac{\Delta_\mathrm{c}(z)}{178}\right]^{1/3} \tag{14}$$

(e.g. Navarro *et al.* 1995; Eke, Cole & Frenk 1996). The temperature $k_\mathrm{B}T = 6.03\,\mathrm{keV}$ for a cluster with $M = 10^{15}\,\mathrm{M}_\odot\,\mathrm{h}^{-1}$ has been adopted from Mathiesen & Evrard (2001). The density parameter at redshift z is denoted by $\Omega(z)$, and Δ_c is the mean overdensity of a virialized sphere,

$$\Delta_\mathrm{c} = 9\pi^2\,\{1 + \alpha\,[\Omega(z) - 1] + \Omega(z)^\beta\} \tag{15}$$

with $(\alpha, \beta) = (0.7076, 0.4403)$ for a flat cosmology (Stöhr 1999). Assuming that the total number N_e of thermal electrons within the cluster virial radius is proportional to the virial mass yields

$$N_\mathrm{e} = \frac{1 + f_\mathrm{H}}{2} f_\mathrm{B} \frac{M}{m_\mathrm{p}}, \tag{16}$$

where f_H is the hydrogen fraction of the baryonic mass ($f_\mathrm{H} \approx 0.76$) and m_p is the proton mass. From X-ray data of an ensemble of 45 clusters, Mohr et al. (1999) derived $f_\mathrm{B} = 0.075\,h^{-3/2}$. Traditionally, the number density of dark matter haloes is described by the Press–Schechter formalism (Press & Schechter 1974). The comoving Press–Schechter mass function can be written as

$$n_\mathrm{PS}(M, z) = \frac{\bar{\rho}}{\sqrt{2\pi}D_+(z)M^2} \left(1 + \frac{n}{3}\right) \left(\frac{M}{M_*}\right)^{(n+3)/6} \times \exp\left[-\frac{1}{2D_+^2(z)} \left(\frac{M}{M_*}\right)^{(n+3)/3}\right], \tag{17}$$

where M_* and $\bar{\rho}$ are the non-linear mass today and the mean background density at the present epoch, and $D_+(z)$ is the linear growth factor of density perturbations, normalized to unity today, $D_+(0) = 1$. $n \approx -1$ denotes the effective exponent of the dark matter power spectrum at the cluster scale. Sheth & Tormen (1999) recently proposed a significantly improved analytic derivation of the mass function while Jenkins et al. (2001) measured the mass function of dark matter haloes in numerical simulations and found a fitting formula very close to that of Sheth & Tormen, however being of slightly lower amplitude at high masses. Thus, the fitting formula found by Jenkins et al. was used in our study.

The total Compton-y parameter per unit solid angle is given by

$$\mathcal{Y}_\Omega = d_\mathrm{A}^2 \int \mathrm{d}^2\theta\; y(\theta) = \frac{k_\mathrm{B}T_\mathrm{e}}{m_\mathrm{e}c^2}\sigma_\mathrm{T}N_\mathrm{e}, \tag{18}$$

where d_A is the angular-diameter distance to the cluster. The mean background level of SZ fluctuations is given by

$$\langle y_\mathrm{bg}\rangle_\theta(z, M_0) = \int \mathrm{d}z \left|\frac{\mathrm{d}V}{\mathrm{d}z}\right| (1+z)^3 \int_{M_0} \mathrm{d}M\, n_\mathrm{PS}(M, z)\mathcal{Y}_\Omega(M, z) = \int \mathrm{d}M \int \mathrm{d}V\; \mathcal{Y}_\Omega(M, z)\, \frac{\mathrm{d}^2N(M, z)}{\mathrm{d}M\,\mathrm{d}V}, \tag{19}$$

where $\mathrm{d}V$ is the cosmic volume per unit redshift and unit solid angle, $n_\mathrm{PS}(M, z)$ is the mass function of collapsed haloes (17) and $\mathcal{Y}_\Omega(M, z)$ is the integrated Compton-y parameter per unit solid angle from (18) expressed in terms of halo mass M and redshift z. Background fluctuations are due to Poisson fluctuations in the number of clusters per unit mass and volume if cluster correlations are neglected. The variance of the background fluctuations reads

$$\left\langle y_\mathrm{bg}^2\right\rangle_\theta(z, M_0) = \int_{M_0} \mathrm{d}M \int \mathrm{d}V\,[\mathcal{Y}_\Omega(M, z)]^2\, \frac{\mathrm{d}^2N(M, z)}{\mathrm{d}M\,\mathrm{d}V}. \tag{20}$$

Fig. 3 shows a qualitative comparison of the influence of the background of unresolved SZ clusters on the mean background level $\langle y_\mathrm{bg}\rangle_\theta(z, M_0)$ and the variance $\langle y_\mathrm{bg}^2\rangle_\theta(z, M_0)$. For studying this influence quantitatively, the ratio of mean background levels and variances is defined via

$$r_\mathrm{mean} = \frac{\langle y_\mathrm{bg}\rangle_\theta(z_\mathrm{sim}, M_\mathrm{sim})}{\langle y_\mathrm{bg}\rangle_\theta(z_\mathrm{max}, M_\mathrm{min})}, \tag{21}$$

$$r_\mathrm{var} = \frac{\left\langle y_\mathrm{bg}^2\right\rangle_\theta(z_\mathrm{sim}, M_\mathrm{sim})}{\left\langle y_\mathrm{bg}^2\right\rangle_\theta(z_\mathrm{max}, M_\mathrm{min})}, \tag{22}$$

where the numerator accounts for the resolved clusters in our simulation with $z < z_\mathrm{sim} = 1.5$ and $M > M_\mathrm{sim} = 5 \times 10^{13}\,\mathrm{M}_\odot\,\mathrm{h}^{-1}$ while the denominator accounts for all collapsed haloes contributing to the SZ flux in our analytic estimate ($z < z_\mathrm{max} = 20$ and $M > M_\mathrm{min} = 1 \times 10^{13}\,\mathrm{M}_\odot\,\mathrm{h}^{-1}$). Performing these integrals yields ratios of $r_\mathrm{mean} = 40.6$ per cent and $r_\mathrm{var} = 93.3$ per cent and thus confirms the qualitative picture of Fig. 3. Therefore, we conclude that we can safely neglect the effect of the background of unresolved SZ

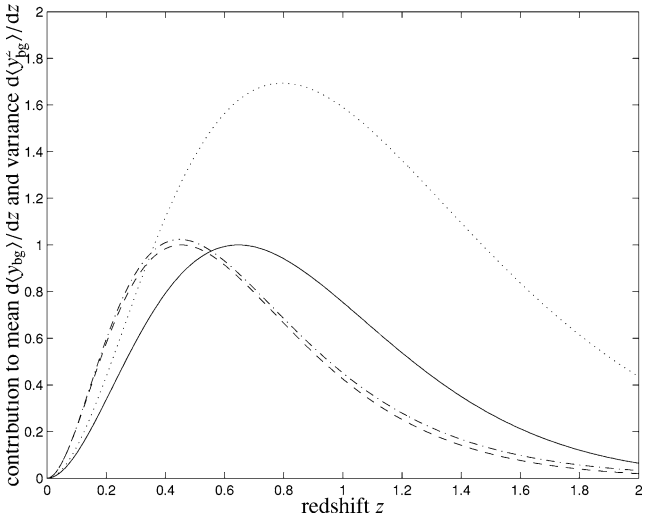

Figure 3. Comparison of the mean background levels $\langle y_\mathrm{bg}\rangle_\theta(z, 5 \times 10^{13}\,\mathrm{M}_\odot\,\mathrm{h}^{-1})$ (solid) and $\langle y_\mathrm{bg}\rangle_\theta(z, 10^{13}\,\mathrm{M}_\odot\,\mathrm{h}^{-1})$ (dotted), the variances $\langle y_\mathrm{bg}^2\rangle_\theta(z, 5 \times 10^{13}\,\mathrm{M}_\odot\,\mathrm{h}^{-1})$ (dashed) and $\langle y_\mathrm{bg}^2\rangle_\theta(z, 10^{13}\,\mathrm{M}_\odot\,\mathrm{h}^{-1})$ (dash–dotted). The differential curves show qualitatively the smaller impact of low-mass and high-redshift clusters on the variance compared to the mean background of SZ fluctuations.

clusters on power spectrum statistics of our SZ all-sky map, especially when considering the mentioned uncertainties in $f_{\rm B}$ and the ionization fraction of electrons in low-mass haloes.

5 RESULTS

This section provides various characterizations of the SZ-cluster sample and properties of the resulting map. First, a visual impression of the SZ maps is given in Section 5.1. Distribution of the angular sizes and of the integrated thermal and kinetic Comptonizations is presented in Sections 5.2 and 5.3, respectively. The distribution of pixel amplitudes and a discussion of the sky-averaged thermal Comptonization are given in Section 5.4. The angular power spectra in comparison to those obtained in high-resolution simulations performed by White et al. (2002) are shown in Section 5.5. Finally, source counts in three relevant *Planck* channels are given in Section 5.6.

In order to quantify the deviations resulting in using template SZ maps instead of relying solely on analytical profiles and idealized scaling relations, the distributions following from the respective approach are contrasted in Section 5.2 (angular sizes), Section 5.3 (integrated Comptonizations) and Section 5.6 (source count at three selected *Planck* frequencies).

5.1 Sky views

In order to give a visual impression of the sky maps, all-sky views in Mollweide projection of the Compton-y parameter (Fig. 4) as well as of the Compton-w parameter (Fig. 5) are presented. Apart from those images, detailed maps of small regions of the SZ sky are presented in Fig. 6 for the thermal and in Fig. 7 for the kinetic SZ effects, respectively. These detailed maps display interesting features: clearly, cluster substructure is visible in the maps, for example, at position $(\lambda, \beta) \simeq (134\overset{\circ}{.}60,\ 45\overset{\circ}{.}25)$.

Secondly, massive clusters that generate a strong thermal signal are rare, such that in drawing a peculiar velocity from a Gaussian distribution large values are less likely to be obtained. Consequently, these clusters commonly show only a weak kinetic signal, a nice example can be found at the position $(\lambda, \beta) \simeq (135\overset{\circ}{.}25, 44\overset{\circ}{.}75)$. Closeby, the inverse example can be found at $(\lambda, \beta) \simeq (135\overset{\circ}{.}40, 44\overset{\circ}{.}50)$, where a low-mass cluster shows only a weak thermal signal, but has sufficient optical depth and a high enough peculiar velocity to give rise to a strong kinetic signal. Finally, at $(\lambda, \beta) \simeq (135\overset{\circ}{.}90, 45\overset{\circ}{.}75)$, there is an example of a merging cluster, with a dipolar variation of the subcluster velocities.

The occurrence of high kinetic SZ amplitudes is a subtle point: cluster velocities follow a Gaussian distribution with mean consistent with zero, because the large-scale structure is at rest in the comoving CMB frame and with a standard deviation of $\sigma_{\upsilon} = 312.8 \pm 0.2\,{\rm km\,s^{-1}}$. This value has been measured for clusters in the Hubble-volume catalogue. As illustrated in Fig. 8, the velocity distribution does *not* depend on the cluster mass because on the scales of typical cluster separation, linear structure formation is responsible for accelerating the clusters to their peculiar velocity. Consequently, the parameters of the Gaussian peculiar velocity distribution (i.e. mean velocity and variance) do not depend on the cluster mass.

More precisely, Hernandez-Monteagudo et al. (2006) derive the velocity dispersion of clusters of galaxies for linear structure formation in a Gaussian random field and find a very weak dependence of velocity dispersion on cluster mass, $\sigma_{\rm vel} \propto M^{-0.13}$. This result suggests a $\lesssim$10 per cent variation of the velocity dispersion for the mass range considered in this analysis, but the evolution of peculiar velocities with decreasing redshift counteracts this tendency by a similar amount.

At first sight, the points in Fig. 8 seem to suggest the contrary, but one has to keep in mind that the clusters form increasingly rarely with increasing mass. This means that with increasing mass a decreasing number of objects have velocities above a certain threshold, i.e. high peculiar velocities are seldom drawn from the underlying Gaussian distribution. In summary, one observes that velocities for clusters are described by a Gaussian distribution whose parameters (mean velocity and velocity dispersion) do not depend on the cluster mass, if marginalized over the cluster masses and redshifts considered here. Only the normalization of this velocity distribution, in

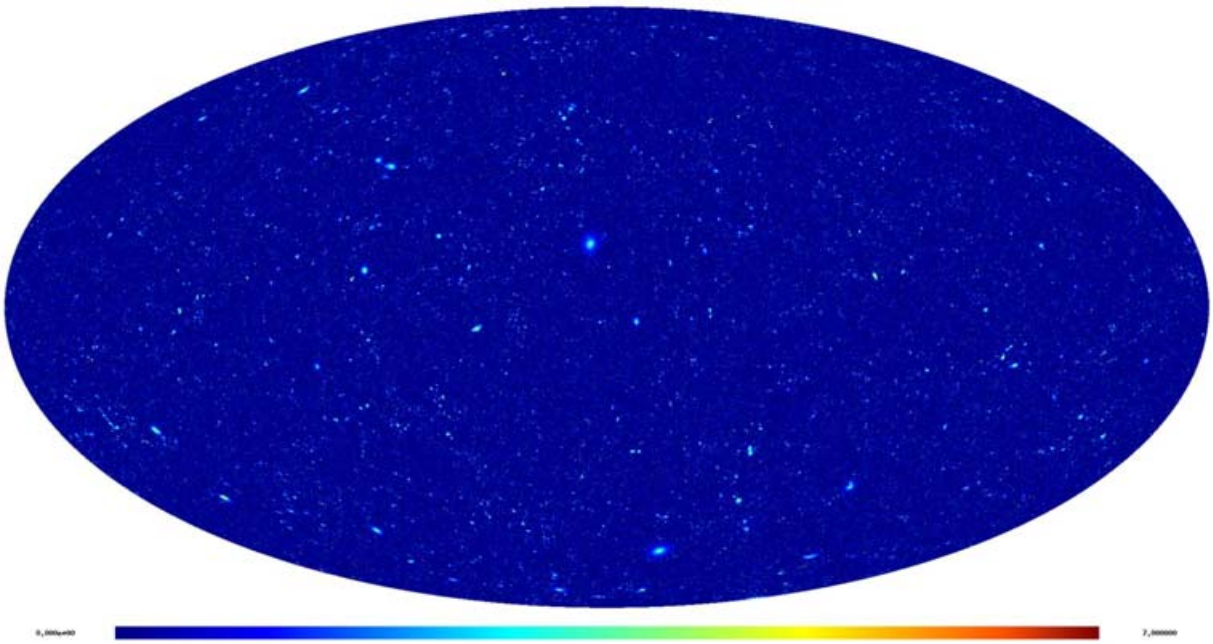

Figure 4. All-sky map of the thermal Comptonization parameter y in Mollweide projection. The shading is proportional to arsinh ($10^6 \times y$).

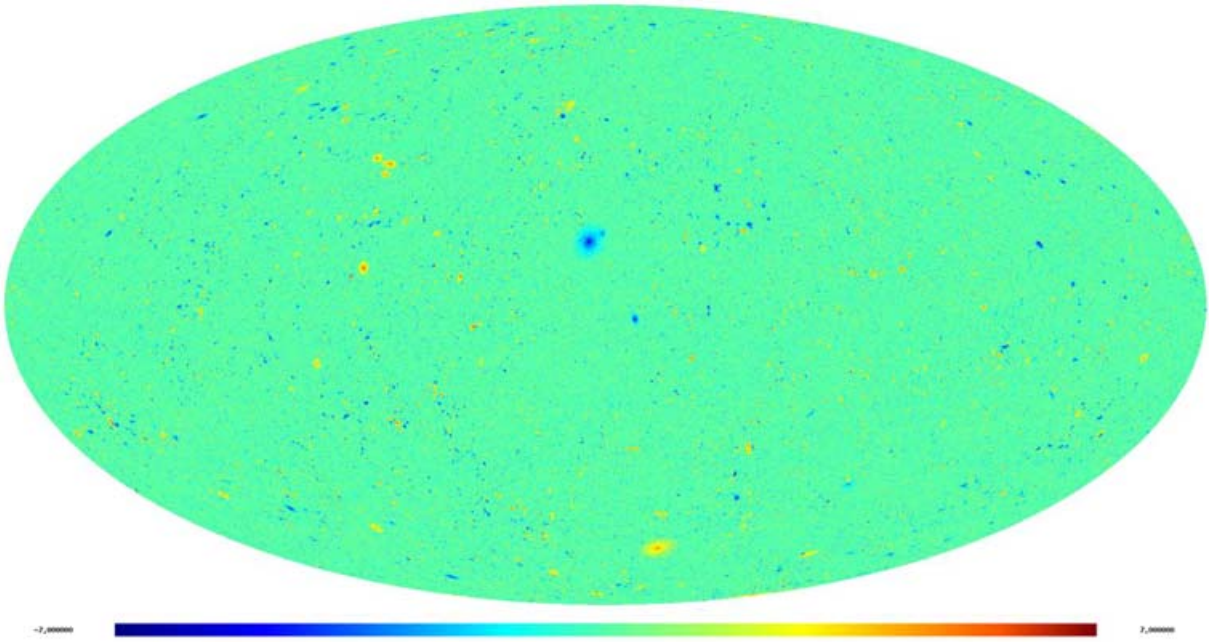

Figure 5. All-sky map of the kinetic Comptonization parameter w in Mollweide projection. The shading is proportional to arsinh $(10^7 \times w)$.

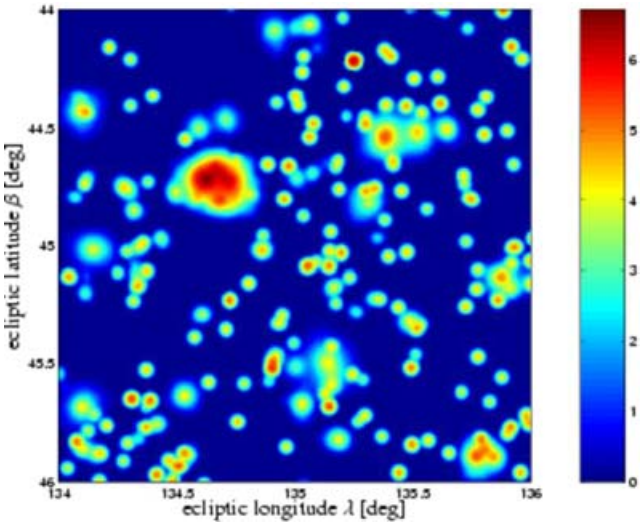

Figure 6. Details of the thermal Comptonization map. A $2^\circ \times 2^\circ$ wide cut-out centred on the ecliptic coordinates $(\lambda, \beta) = (135^\circ, 45^\circ)$ is shown. The smoothing imposed was a Gaussian kernel with $\Delta\theta = 2.0$ arcmin (FWHM). The shading indicates the value of the thermal Comptonization y and is proportional to arsinh $(10^6 \times y)$. This map resulted from a projection on a Cartesian grid with mesh size $\sim$14 arcsec, i.e. no HEALPIX pixelization can be seen.

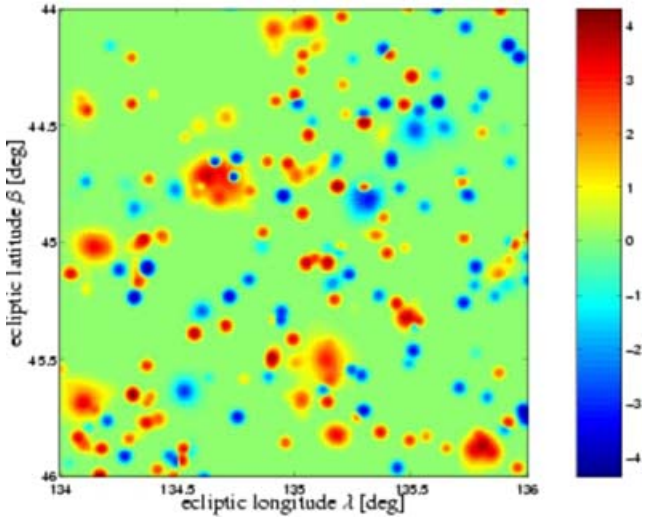

Figure 7. Details of the kinetic Comptonization map. A $2^\circ \times 2^\circ$ wide cut-out centred on the same position as Fig. 6, i.e. at the ecliptic coordinates $(\lambda, \beta) = (135^\circ, 45^\circ)$, is shown. The smoothing imposed was a Gaussian kernel with $\Delta\theta = 2.0$ arcmin (FWHM). The kinetic Comptonization w is indicated by the shading which is proportional to arsinh $(10^6 \times w)$.

fact, decreases with increasing mass, because massive objects are rare.

Despite the seemingly large separation, it would be incorrect to draw the velocities independently from a Gaussian distribution. Instead, the kinetic SZ map ensures the consistency that the density and velocity fields have grown from the initial Gaussian random field by linear structure formation and have the correct relative phases.

Similar to the clustering on large angular scales that the thermal SZ map shows due to the formation of superclusters, the kinetic SZ map is expected to exhibit clustering on the same angular scales. This is because in the formation of superclusters, the velocity vectors of infalling clusters point at the dynamical centre and are thus correlated despite the large separation.

5.2 Distribution of angular sizes

The distribution of cluster sizes is an important characteristic of the sky maps. For the derivation of core sizes, two different paths have been pursued in order to contrast the ideal case, in which cluster sizes follow from the well-known virial relations to the simulated and realistic case, in which the sizes are measured on the template maps themselves. First, the cluster sizes are measured on the data

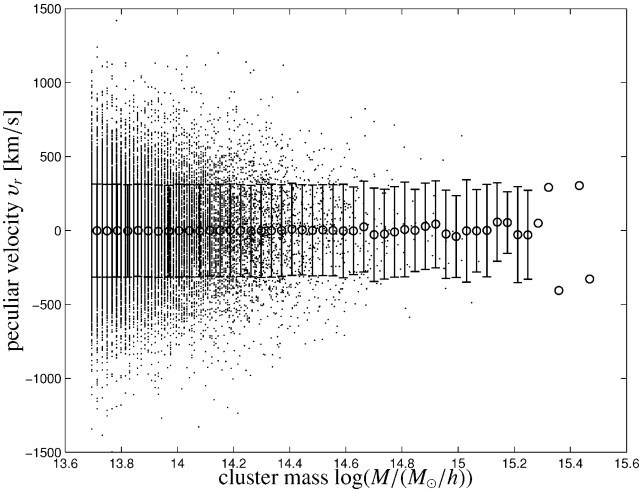

Figure 8. Mean value and variance of the (Gaussian) distribution of peculiar velocities v_r as a function of cluster mass M. The parameters of the distribution do not depend on mass, i.e. the mean is consistent with zero and the standard deviation has values $\simeq$320 km s^{-1} irrespective of mass. Standard deviations for the five bins corresponding to the largest cluster masses have been omitted due to poor statistics. The underlying data points represent 1 per cent randomly selected entries of the Hubble-volume catalogue.

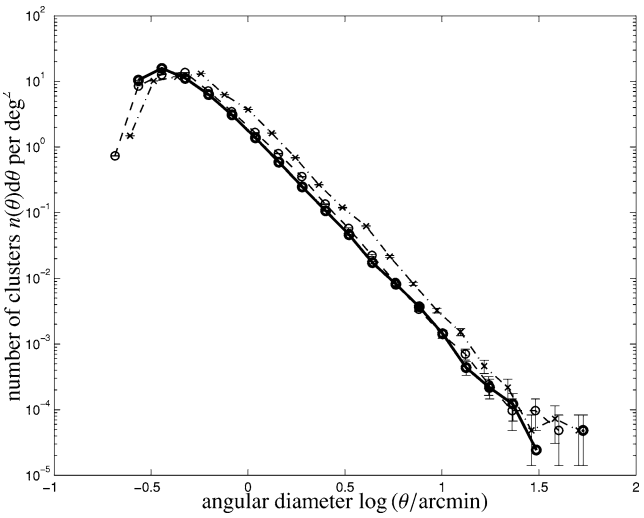

Figure 9. The number of clusters $n(\theta)\,\mathrm{d}\theta$ per square degree for a given angular diameter θ is shown without taking beam convolution into account for thermal clusters (circles, dashed line) and kinetic clusters (crosses, dash–dotted line) as following from β-model fits to template data. For comparison, the distribution of angular diameters obtained via the virial theorem (solid line) is also plotted.

by fitting a King profile (Cavaliere & Fusco-Femiano 1978) to the thermal and kinetic template maps:

$$y(\boldsymbol{r}) = y_0 \left[1 + \left(\frac{|\boldsymbol{r}|}{r_{\mathrm{c}}^{(y)}}\right)^2\right]^{-1} \tag{23}$$

$$w(\boldsymbol{r}) = w_0 \left[1 + \left(\frac{|\boldsymbol{r}|}{r_{\mathrm{c}}^{(w)}}\right)^2\right]^{-1}, \tag{24}$$

yielding the core radii $r_{\mathrm{c}}^{(y)}$ for the thermal and $r_{\mathrm{c}}^{(w)}$ for the kinetic map, respectively. The β-fits have been centred on the pixel with the highest amplitude, and as free parameters only the central amplitudes y_0 and w_0 were used apart from the core radii. The resulting radii have been averaged over all three projections of the cluster. Together with the comoving distance of the cluster, as given by the Hubble-volume catalogue and the scaling factor required to match the size (compare Section 4.2), the core radii have been converted into angular diameters.

Secondly, an angular extent has been derived from the virial radius. Template data suggest the relation

$$r_{\mathrm{c}} \simeq 0.12\, r_{\mathrm{vir}} \tag{25}$$

rather than the value of $r_{\mathrm{c}} \simeq 0.07 r_{\mathrm{vir}}$ advocated by Lloyd-Davies, Ponman & Cannon (2000) and Kay et al. (2001). In analogy, the angular diameter was then determined with the cluster distance given by the Hubble-volume catalogue.

In Fig. 9, the size distributions for the thermal as well as for the kinetic clusters are given. Clearly, most clusters have small angular diameters compared to *Planck*'s beam, and would appear as point sources. Here, it should be emphasized that the HEALPIX tesselation with the chosen N_{side}-parameter does not resolve structures smaller than 1.71 arcmin. In the process of smoothing the clusters imposed prior to projection (compare Section 4.3), clusters with diameters smaller than 2.0 arcmin have been replaced by two-dimensional Gaussians with $\sigma = 2.0$ arcmin. Their normalization corresponds to the integrated Comptonizations $\mathcal{Y}$ and $\mathcal{W}$ measured on the template maps. The smoothing is an absolute necessity because otherwise the HEALPIX map would need $\sim 10^4$ times as many pixels for supporting the most distant and hence smallest clusters in the Hubble sample and hence $\sim 10^4$ times the storage space. A further point to note is the remarkably good agreement between diameters derived from the various prescriptions.

5.3 Distribution of the integrated thermal and kinetic Comptonization

The signal strength of a cluster in a SZ observation is not given by the line-of-sight Comptonization, but rather by the Comptonization integrated over the solid angle subtended by the cluster. These quantities are referred to as the integrated thermal Comptonization $\mathcal{Y}$ and kinetic Comptonization $\mathcal{W}$ and are defined as

$$\mathcal{Y} = \int \mathrm{d}\Omega\, y(\boldsymbol{\theta}) \quad \text{and} \quad \mathcal{W} = \int \mathrm{d}\Omega\, w(\boldsymbol{\theta}). \tag{26}$$

For a simple model of the integrated Comptonizations as functions of cluster mass M, distance z and peculiar velocity v_r, it is assumed that the SZ flux originates from inside a sphere of radius r_{vir}, the baryon fraction is equal to its universal value $f_{\mathrm{B}} = \Omega_{\mathrm{B}}/\Omega_{\mathrm{M}}$ and the ICM is completely ionized and has a uniform temperature predicted by the spherical collapse model laid down in equation (14). In this model, the actual distribution of electrons inside the virial sphere is of no importance. Then, the integrated Comptonizations are approximated by

$$\frac{\mathcal{Y}_{\mathrm{vir}}}{\mathrm{arcmin}^2} = 1.98\, \frac{f_{\mathrm{B}}}{h} \left(\frac{M_{\mathrm{vir}}}{M_\star}\right)^{\frac{5}{3}} \left(\frac{d_{\mathrm{A}}}{d_\star}\right)^{-2} \times (1+z) \left(\frac{\Omega_0}{\Omega}\right)^{\frac{1}{3}} \left(\frac{\Delta_{\mathrm{c}}}{178}\right)^{\frac{1}{3}}, \tag{27}$$

$$\frac{\mathcal{W}_{\mathrm{vir}}}{\mathrm{arcmin}^2} = 0.29\, \frac{f_{\mathrm{B}}}{h} \left(\frac{M_{\mathrm{vir}}}{M_\star}\right) \left(\frac{d_{\mathrm{A}}}{d_\star}\right)^{-2} \left(\frac{v_{\mathrm{r}}}{v_\star}\right), \tag{28}$$

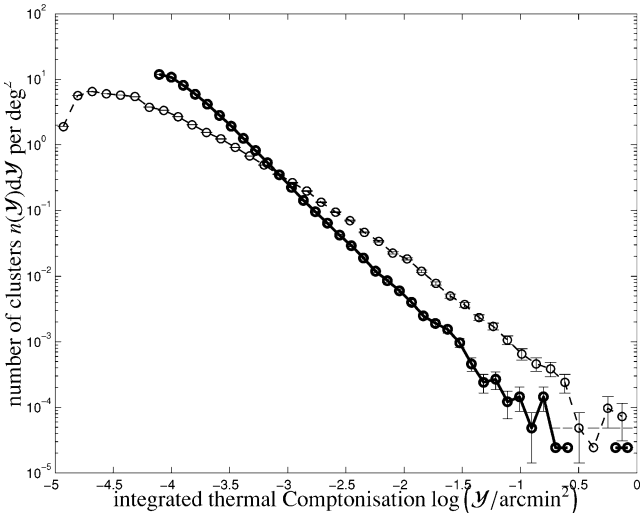

Figure 10. The number of clusters $n(\mathcal{Y})\,\mathrm{d}\mathcal{Y}$ per square degree for given integrated thermal Comptonization $\mathcal{Y}$ derived from template data (dashed line) in comparison to the analogous quantity based on virial estimates (solid line).

respectively. The reference values have been chosen to be $M_\star = 10^{15}\,\mathrm{M}_\odot\,\mathrm{h}^{-1}$, $d_\star = 100\,\mathrm{Mpc\,h}^{-1}$ and $\upsilon_\star = 1000\,\mathrm{km\,s}^{-1}$. d_A is the angular diameter distance to the cluster. $\Omega = \Omega(z)$ denotes the mass density at redshift z and $\Delta_\mathrm{c} = \Delta_\mathrm{c}(z)$ the overdensity of a virialized sphere, an approximate description is given by equation (15). For typical values for mass, distance and velocity, the thermal and kinetic SZ effects differ by approximately one order of magnitude. The baryon fraction is set to the universal value $f_\mathrm{B} = \Omega_\mathrm{B}/\Omega_\mathrm{M} = 0.133$ for the remainder of this paper.

Distributions of the integrated thermal and kinetic Comptonizations are shown in Figs 10 and 11, respectively. The distributions have been derived from actual scaled template data in comparison to the values obtained from (27) and (28).

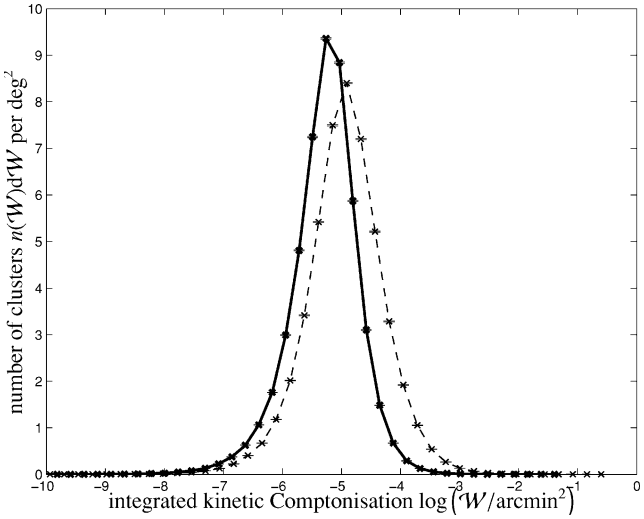

Figure 11. The number of clusters $n(\mathcal{W})\,\mathrm{d}\mathcal{W}$ per square degree for given integrated kinetic Comptonization $\mathcal{W}$ derived from template data (dashed line) in comparison to the analogous quantity based on virial estimates (solid line). Here, the scaling of the vertical axis is linear, in contrast to Fig. 11, such that the underlying Gaussian distribution of peculiar velocities becomes apparent.

Fig. 10 shows the number of clusters per square degree with integrated thermal Comptonization $\mathcal{Y}$. It can be seen that the approach relying on the virial theorem underestimates the number of cluster by a factor of 2–3 for large integrated Comptonizations. Alternatively, one could state that the distributions are separated at high Comptonizations by slightly less than 0.5 dex. The reason for the significantly larger integrated Comptonizations determined from template data is due to the fact that the template clusters were matched to the catalogue entries given by the Hubble-volume simulation by their virial masses. In irregular clusters, there is a significant fraction of the gas located outside the virial sphere, and thus the integrated Comptonization is systematically underestimated when applying a spherical overdensity code to simulation data, as previously examined in Fig. 2. In scaling the template clusters up to the masses required by the Hubble-volume catalogue, this difference is amplified because in the sparsely sampled region of the M–z-diagram (compare Figs 1 and 2) clusters have on average to be scaled to higher masses, which explains the offset in the distributions.

A second effect is the evolution of ICM temperature. Compared to the temperature model equation (14) based on spherical collapse theory, the plasma temperatures are smaller by approximately 25 per cent, i.e. the mean SPH temperature of the particles inside the virial sphere is smaller than expected from spherical collapse theory and reflects the departure from isothermality. The template clusters do show a temperature profile that declines towards the outskirts of the clusters, which decreases the integrated Comptonization relative to the values derived by means of the virial theorem.

Furthermore, the dependence of electron temperature on cluster mass is notably weaker than the $M^{2/3}$-scaling. The cluster number weighted average for the exponent α in the scaling $T \propto M^\alpha$ relating temperature to mass was found to be $\langle\alpha\rangle = 0.624$, and at the redshifts around unity, where most of the clusters reside, values as small as $\alpha = 0.605$ were derived. Using this scaling, the Compton-y parameter, and hence the integrated thermal Comptonization $\mathcal{Y}$, shows a significantly shallower distribution compared to the distribution relying on simple scaling arguments.

The same argument applies to the kinetic Comptonization $\mathcal{W}$, as depicted in Fig. 11. Here, a shifting of the values to smaller kinetic Comptonizations is observed when comparing estimates following from the virial theorem to actual simulation data. The shift of the peak of the distribution amounts to about one-third dex, as explained above for the thermal Comptonizations. Keeping the $M^{\frac{5}{3}}$-scaling of the thermal SZ effect in mind, the shift in the $\mathcal{W}$-distribution is then consistent with the shift of the $\mathcal{Y}$-distribution.

5.4 Distribution of Comptonization per pixel

Fig. 12 shows the distribution of the pixel amplitudes of the thermal SZ map as well as of their absolute values in the kinetic SZ map. Clearly, the kinetic and thermal SZ effects are separated by approximately one order of magnitude.

The distribution of pixel amplitudes is very broad, encompassing the largest line-of-sight Comptonizations of $y \simeq 1.5 \times 10^{-4}$ and $|w| \simeq 1.6 \times 10^{-5}$ down to very low signals below $\log(y) \simeq -20$. The distribution is bimodal, which is a pixelization artefact and which is caused by the replacement of faint and small clusters with a very narrow Gaussian, the extent of which is slightly above the pixel scale, once the cluster is smaller than $\simeq$2.0 arcmin in diameter. These clusters are more concentrated than the King profiles of resolved clusters. There is a caveat when applying an expansion into spherical harmonics $Y^\ell_m(\boldsymbol{\theta})$ to the SZ maps. The smallest clusters are only

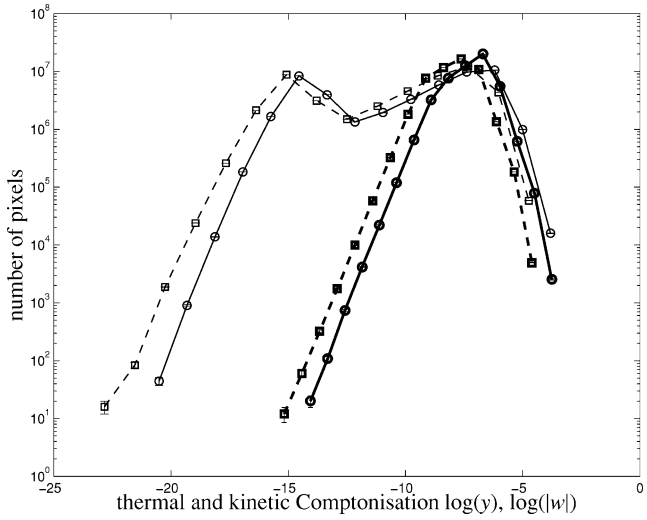

Figure 12. Distribution of pixel amplitudes of the thermal Comptonization parameter y (circles, solid) and the absolute value of the kinetic Comptonization $|w|$ (squares, dashed). Zero values have been deliberately excluded. The figure illustrates the occurrence of clusters comparable to the HEALPIX pixel scale. The thin set of lines shows an additional peak at small Comptonizations that vanish after convolution with a beam of $\Delta\theta = 5.0$ arcmin (FWHM), i.e. comparable to *Planck*, as shown by the thick lines.

a few pixels in diameter. Working with the HEALPIX tesselation, reliable expansion coefficients can only be obtained up to multipole moments of the order of $\ell \simeq 2 \times N_{\rm side}$, i.e. up to $\ell \simeq 4096$ in our case, which corresponds to angular scales of 2.64 arcmin. The pixel scale is 1.71 arcmin for this choice of the $N_{\rm side}$-parameter. Consequently, the small clusters will not be contained in an expansion into spherical harmonics, as shown by the set of thick lines in Fig. 12. Here, the map has been decomposed in $a_{\ell m}$-coefficients (compare equation 31), multiplied with the $a_{\ell 0}$-coefficients of a Gaussian beam of $\Delta\theta =$ 5.0 arcmin [full width at half-maximum (FWHM)] and synthesized again. Then, the resulting smoothed map does not contain small clusters, because the decomposition into spherical harmonics has not been able to resolve structures that extend over only a few pixels.

The mean value of the thermal Comptonization y has been determined to be $\langle y\rangle = 3.01 \times 10^{-7}$ and the pixel-to-pixel variance is $\sigma_y = \sqrt{\langle y^2\rangle - \langle y\rangle^2} = 1.85 \times 10^{-6}$. In analogy, the value $\langle w\rangle = 6.28 \times 10^{-9}$ has been derived for the kinetic map, with variance $\sigma_w = \sqrt{\langle w^2\rangle - \langle w\rangle^2} = 3.78 \times 10^{-7}$, i.e. the mean kinetic Comptonization is consistent with zero, due to the peculiar velocities following a Gaussian distribution with zero mean. The mean value of the moduli of the pixel amplitudes of the kinetic map is $\langle |w|\rangle = 7.65 \times 10^{-8}$.

The value for the mean Comptonization $\langle y\rangle$ measured on the map should account for roughly 40 per cent of the mean thermal Comptonization as derived in Section 4.4 due to the lower mass threshold inherent to the simulation. Keeping in mind the absence of any diffuse component of the thermal Comptonization, the value derived here is compatible with the value of $\simeq 10^{-6}$ given by Refregier et al. (2000) and Scaramella, Cen & Ostriker (1993), but falls short of the value derived by White et al. (2002) by a factor of less than 2. Myers et al. (2004) performed a cross-correlation of *WMAP* data with clusters from the Automated Plate Measurement (APM) survey and found the mean Comptonization to be significantly larger and in accordance with Persi et al. (1995), but in contradiction with expectations from CDM models.

5.5 Angular power spectra of the thermal and kinetic SZ effects

In this section, the angular power spectra are given for the all-sky maps. They follow from a decomposition of the spherical data set into spherical harmonics $Y_\ell^m(\boldsymbol{\theta})$:

$$y_{\ell m} = \int_{4\pi} {\rm d}\Omega\, y(\boldsymbol{\theta})\, Y_\ell^m(\boldsymbol{\theta})^*, \tag{29}$$

$$w_{\ell m} = \int_{4\pi} {\rm d}\Omega\, w(\boldsymbol{\theta})\, Y_\ell^m(\boldsymbol{\theta})^* \text{and} \tag{30}$$

$$w'_{\ell m} = \int_{4\pi} {\rm d}\Omega\, |w(\boldsymbol{\theta})|\, Y_\ell^m(\boldsymbol{\theta})^*, \tag{31}$$

respectively. The spherical harmonical transform $w\prime_{\ell m}$ has been determined from the absolute values of the kinetic map amplitudes. The reason for doing so is the vanishing expectation value of the peculiar velocities in the comoving frame such that for a given cluster in the thermal SZ map, both signs of the kinetic SZ effect are equally likely to occur and the cross-power averages out to zero. The angular power spectra and the cross-power spectrum are defined via

$$C_{yy}(\ell) = \frac{1}{2\ell+1} \sum_{m=-\ell}^{+\ell} y_{\ell m}\, y_{\ell m}^*, \tag{32}$$

$$C_{ww}(\ell) = \frac{1}{2\ell+1} \sum_{m=-\ell}^{+\ell} w_{\ell m}\, w_{\ell m}^*, \tag{33}$$

$$C_{yw'}(\ell) = \frac{1}{2\ell+1} \sum_{m=-\ell}^{+\ell} w'_{\ell m}\, y_{\ell m}^*, \tag{34}$$

with the asterisk denoting complex conjugation. The resulting power spectra are given in Fig. 13 in comparison to the power spectra derived by White et al. (2002) in simulations covering smaller angular scales. The curves match well, and the remaining discrepancies may be explained by the fact that in the maps presented here, power is missing on small scales due to the low-M high-z cut-off, whereas the simulation by White is missing power on large scales due to the smallness of their simulation box. The bending-over of the spectra derived from our SZ maps is also due to the fact that the expansion in spherical harmonics cannot be computed for angular scales approaching the pixel scale and thus does not include very small clusters of sizes comparable to the pixel size, as already discussed in Section 5.4.

It is difficult to assign error bars to the angular power spectrum depicted in Fig. 13, because only one realization of the Hubble volume is available. Simple cosmic variance error bars $\sigma[C(\ell)] = \sqrt{2/(2\ell+1)}C(\ell)$ are not applicable because the SZ effect cannot be represented by a Gaussian random field. The limiting step, however, would be numerics in the spherical harmonical transform, and here the detrended fluctuation of the $y_{\ell m}$-coefficients about their bandpass average $C(\ell)$ amounts to roughly 0.2 dex at low multipoles.

If clusters were randomly positioned point sources on the sky, the number of clusters per solid angle element would be a Poisson process and the resulting power spectrum should be flat, i.e. $C(\ell) \propto N$ (N is the number of sources), as shown by Seljak, Burwell & Pen (2001). In our spectra, we find a significant deviation in the slope of the power spectra $C(\ell) \propto \ell^{-\gamma}$ as a function of ℓ. The measured slope is $2 + \gamma = 1.53 \pm 0.07$ for the thermal and $2 + \gamma = 1.45 \pm 0.07$ for the kinetic SZ effect, which reflects the deviation from pure

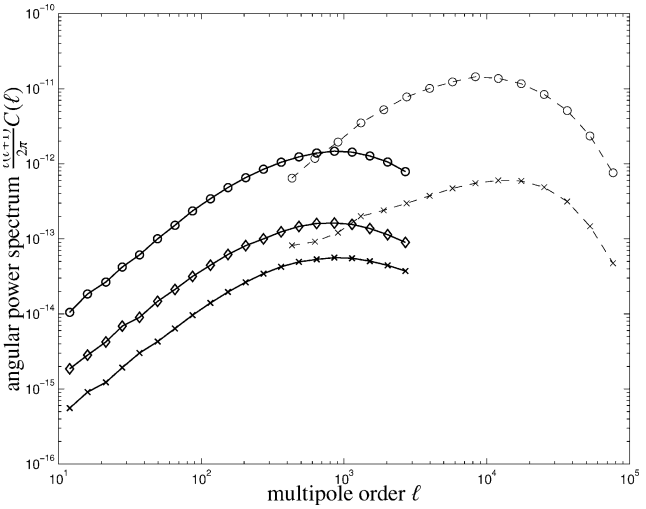

Figure 13. Angular power spectra of the thermal and kinetic SZ effect. $C_{yy}(\ell)$ (circles, solid line), $C_{ww}(\ell)$ (crosses, solid line) and the cross-power spectrum $C_{yw'}(\ell)$ (diamonds, solid line) are shown in comparison to the power spectra of the thermal SZ effect (circles, dashed line) and the kinetic SZ effect (crosses, dashed line) obtained by White et al. (2002) at smaller scales, i.e. at higher multipole order ℓ. The maps are smooth on a scale of 2.0 arcmin, which causes the drop in power at inverse angular scales of $\gtrsim 10^3$.

Poissonianity. In the fitting, the values for ℓ have been restricted to $1 \leqslant \ell \leqslant 100$ and the errors derived correspond to the 95 per cent confidence intervals.

Komatsu & Seljak (2002) give curves for the derivatives $\mathrm{d}\ln C(\ell)/\mathrm{d}\ln M$ and $\mathrm{d}\ln C(\ell)/\mathrm{d}\ln z$ which allow the quantification of the completeness of the power spectrum with respect to cuts in mass M and redshift z. From their analysis, one can conclude that only the smallest multipoles of our SZ spectrum are complete, but there are deficiencies of ∼20 per cent in $C(\ell = 1000)$ and ∼50 per cent in $C(\ell = 3000)$ due the cut in redshift ($z \lesssim 1.5$). Concerning the mass cut ($M \gtrsim 5 \times 10^{13}\,\mathrm{M}_\odot\,\mathrm{h}^{-1}$), the deficiencies in the spectrum amount to roughly ∼10 per cent at $C(\ell = 2000)$ and ∼50 per cent at $C(\ell = 10^4)$. This systematic underdetermination of the spectrum with increasing multipole order ℓ explains the deviation from the Poissonian slope of two described above. Furthermore, the local SZ effect (Dolag et al. 2005) lifts the power spectrum by 0.25 dex due to the influence of near low-mass haloes. The turnover of the spectra at high multipoles is due to the convolution of the scales SZ templates with a Gaussian kernel with 2.0 arcmin width prior to the projection on to the celestial sphere (cf. Section 4.3).

Furthermore, Fig. 13 shows the cross-correlation between the thermal SZ map and the absolute value of the kinetic SZ map. As expected, the amplitude of the cross-power spectrum is at an intermediate level compared to autocorrelations of the thermal and kinetic SZ maps.

Comparing our angular power spectrum to the results of a halo model as worked out by Ma & Fry (2002) or Komatsu & Seljak (2002) is an interesting point. At low multipoles of, for example, $\ell = 100$, i.e. on angular scales where the variance of our map has been shown to be almost complete, we measure amplitudes of $\ell(\ell+1)C(\ell)/(2\pi) \simeq 10^{-12}$ for the choice of cosmological parameters $\sigma_8 = 0.9$ and $\Omega_\mathrm{M} = 0.3$. This value is smaller compared to values found using the halo model by slightly less than half an order of magnitude, but well in agreement with the finding of hydrodynamical simulations (e.g. Refregier et al. 2000; Springel, White & Hernquist 2001). Contrarily, the slope of the spectra in Fig. 13 corresponds well to slope, and, similar to the interpretation of results obtained in hydrosimulation, the lack in amplitude is likely to be due to sampling variance. The same argumentation applies to the kinetic SZ effect, as discussed, for example, by Ma & Fry (2002), in a comparison of our data to a halo model.

5.6 Source counts at *Planck* frequencies

As the last point in this analysis, we address the SZ source counts, i.e. the number N of SZ clusters giving rise to flux changes exceeding a certain flux threshold S_min. The SZ flux modulation as a function of frequency is given by

$$S(x) = S_0 \int \mathrm{d}\Omega\ [y\, g(x) - \beta\tau\, h(x)] \tag{35}$$

$$= S_0\,[\mathcal{Y} g(x) - \mathcal{W} h(x)] = S_\mathcal{Y}(x) - S_\mathcal{W}(x), \tag{36}$$

where $S_0 = 22.9\,\mathrm{Jy\,arcmin}^{-2}$ is the flux density of the CMB and $\mathcal{Y}$ and $\mathcal{W}$ denote the integrated thermal and kinetic Comptonizations. The functions $g(x)$ and $h(x)$ are the flux modulations caused by the thermal and kinetic SZ effects for non-relativistic electron velocities:

$$g(x) = \frac{x^4 \exp(x)}{[\exp(x)-1]^2}\left[x\frac{\exp(x)+1}{\exp(x)-1} - 4\right], \tag{37}$$

$$h(x) = \frac{x^4 \exp(x)}{[\exp(x)-1]^2}. \tag{38}$$

Here, x again denotes the dimensionless frequency $x = h\nu/(k_\mathrm{B} T_\mathrm{CMB})$. The averaged flux $\langle S\rangle_{\nu_0}$ at the fiducial frequency ν_0 is obtained by weighted summation with the frequency response window function $R_{\nu 0}(\nu)$ and can readily be converted to antenna temperature T_A by means of equation (39):

$$\langle S\rangle_{\nu_0} = \frac{\int \mathrm{d}\nu\, S(\nu)\, R_{\nu_0}(\nu)}{\int \mathrm{d}\nu\, R_{\nu_0}(\nu)} = 2\frac{\nu_0^2}{c^2}\, k_\mathrm{B}\, T_\mathrm{A}. \tag{39}$$

The main characteristics of *Planck*'s receivers and the conversion factors from 1 arcmin^2 of thermal or kinetic Comptonization to fluxes in Jansky and changes in antenna temperature measured in nK is given in Table 2. For the derivation of the values, a top-hat shaped frequency response function $R_{\nu 0}(\nu)$ has been assumed:

$$R_{\nu_0}(\nu) = \begin{cases} 1, \nu \in [\nu_0 - \Delta\nu, \nu_0 + \Delta\nu] \\ 0, \nu \notin [\nu_0 - \Delta\nu, \nu_0 + \Delta\nu] \end{cases}. \tag{40}$$

Figs 14–16 show the source counts stated in number of clusters per square degree as a function of averaged flux $\langle S\rangle_{\nu_0}$ for *Planck*'s $\nu_0 = 143$, 217 and 353 GHz channels, respectively.

The source counts $N(S)$ are well approximated by power laws of the form:

$$N(\langle S\rangle > S_\mathrm{min}) = N_0\, S^\alpha. \tag{41}$$

Values for the normalizations N_0 and the slopes α have been obtained by fits to the source counts for the three relevant *Planck* frequencies and are stated in Table 3. In the fits, the four rightmost bins have been excluded because of poor statistics. The parameters of the power law have been derived for the fluxes following from the idealized case based on the virial theorem and compared to fluxes determined from template cluster data.

The slopes derived from fits to the cluster number counts are slightly steeper for the virial estimates compared to template data ($\alpha \simeq -5/3$ versus -1.4), which again reflects the weaker dependence on cluster mass observed in template data. Comparing data

Table 2. Characteristics of *Planck*'s low frequency instrument (LFI) and high frequency instrument (HFI) receivers: centre frequency ν, frequency window $\Delta\nu$ (as defined in equation 40), fluxes $\langle S_{\mathcal{Y}}\rangle$ and $\langle S_{\mathcal{W}}\rangle$ (see equation 36) generated by the respective Comptonization of $\mathcal{Y} = \mathcal{W} = 1$ arcmin^2 and the corresponding changes in antenna temperature $\Delta T_{\mathcal{Y}}$ and $\Delta T_{\mathcal{W}}$. Due to *Planck*'s symmetric frequency response window, the thermal SZ effect does not vanish entirely at ν = 217 GHz.

Planck channel	1	2	3	4	5	6	7	8	9
Centre frequency ν_0	30 GHz	44 GHz	70 GHz	100 GHz	143 GHz	217 GHz	353 GHz	545 GHz	857 GHz
Frequency window $\Delta\nu$	3.0 GHz	4.4 GHz	7.0 GHz	16.7 GHz	23.8 GHz	36.2 GHz	58.8 GHz	90.7 GHz	142.8 GHz
Thermal SZ flux $\langle S_{\mathcal{Y}}\rangle$	−12.2 Jy	−24.8 Jy	−53.6 Jy	−82.1 Jy	−88.8 Jy	−0.7 Jy	146.0 Jy	76.8 Jy	5.4 Jy
Kinetic SZ flux $\langle S_{\mathcal{W}}\rangle$	6.2 Jy	13.1 Jy	30.6 Jy	55.0 Jy	86.9 Jy	110.0 Jy	69.1 Jy	15.0 Jy	0.5 Jy
Antenna temperature $\Delta T_{\mathcal{Y}}$	−440 nK	−417 nK	−356 nK	−267 nK	−141 nK	−0.5 nK	38 nK	8.4 nK	0.2 nK
antenna temperature $\Delta T_{\mathcal{W}}$	226 nK	220 nK	204 nK	179 nK	138 nK	76 nK	18 nK	1.6 nK	0.02 nK

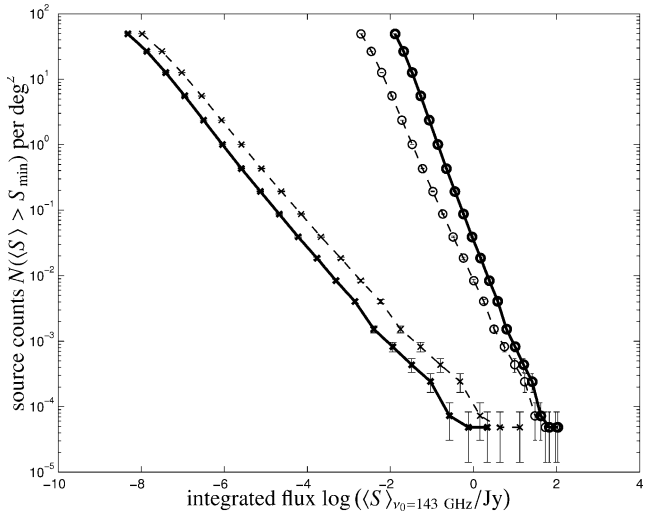

Figure 14. Source counts $N(\langle S\rangle > S_{\rm min})$ for thermal (circles) and kinetic clusters (crosses) for *Planck*'s $\nu_0 = 143$ GHz channel and for fluxed measured on the scaled template clusters (dashed line) in comparison to virial fluxes (solid line).

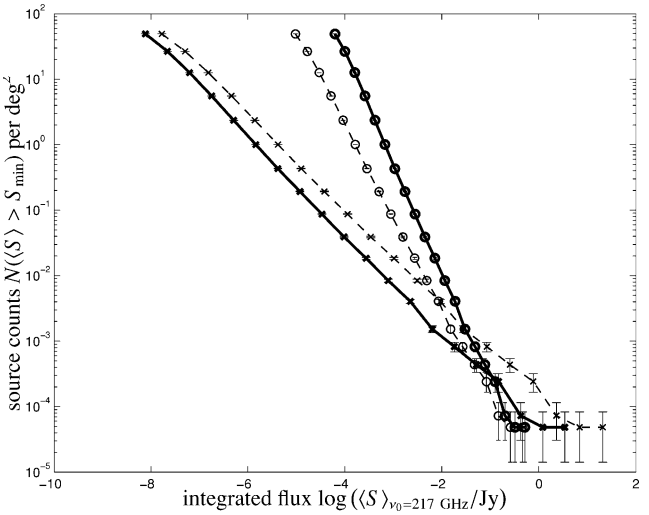

Figure 15. Source counts $N(\langle S\rangle > S_{\rm min})$ for thermal (circles) and kinetic clusters (crosses) for *Planck*'s $\nu_0 = 217$ GHz channel, the dashed and solid lines contrast the fluxes measured on the template data and those following from virial scaling relations, respectively. For the given frequency response function $R_{\nu 0}(\nu)$, the thermal SZ effect does not vanish entirely at $\nu_0 = 217$ GHz.

sets for different frequencies, the slopes α are, of course, almost identical, because only amplitudes are changed by the choice of a different frequency band. The number of clusters N_0 stays roughly constant in the case of the kinetic SZ effect, but reflects the distinct frequency modulation in the case of the thermal SZ effect. Here, it should be emphasized that the thermal SZ effect does not vanish entirely at $\nu = 217$ GHz due to *Planck*'s symmetric frequency response window. The difference in numbers between the estimates based on virial quantities to those measured on template data amounts to roughly half an order of magnitude in the kinetic SZ effect, but rises almost an order of magnitude at small fluxes for the thermal SZ effect. There is, however, good agreement in the number counts of thermal SZ clusters at high fluxes.

The difference in slope of the thermal versus kinetic SZ cluster number counts is caused by the $M^{5/3}$-scaling of the thermal SZ effect relative to the proportionality to M of the kinetic effect. Due to the difference in slope, the effects are separated by two orders of magnitude for the largest fluxes, while this difference increases to eight orders of magnitude for the smallest fluxes, which hints at the difficulties to be faced in detecting kinetic clusters compared to even faint thermal detections. The slopes derived here are in good agreement with the those obtained by Kay et al. (2001).

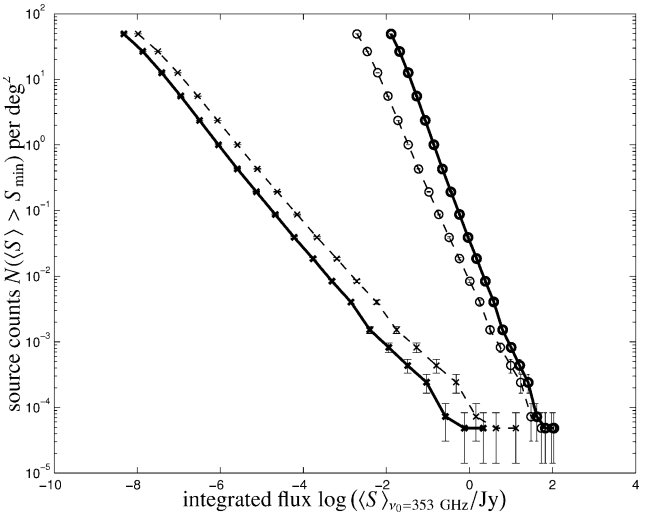

Figure 16. Source counts $N(\langle S\rangle > S_{\rm min})$ for thermal (circles) and kinetic clusters (crosses) for *Planck*'s $\nu_0 = 353$ GHz channel, again for fluxes derived from template data (dashed line) in comparison to fluxes following from virial scaling relations (solid line).

Table 3. Values obtained from fits of a power law of the type $N(S) = N_0 S^{\alpha}$ to the cumulative source counts as a function of flux exceeding the threshold S for both SZ effects. In the table, values obtained from virial estimates are contrasted to values following from measurements on template data. The errors quoted denote the 95 per cent confidence intervals.

Planck channel	$\nu_0 = 143$ GHz	$\nu_0 = 217$ GHz	$\nu_0 = 353$ GHz
Thermal SZ effect, virial estimate	$\log N_0 = -1.78 \pm 0.02$	$\log N_0 = -5.31 \pm 0.02$	$\log N_0 = -1.42 \pm 0.22$
	$\alpha = -1.67 \pm 0.03$	$\alpha = -1.67 \pm 0.07$	$\alpha = -1.66 \pm 0.02$
Kinetic SZ effect, virial estimate	$\log N_0 = -4.49 \pm 0.01$	$\log N_0 = -4.42 \pm 0.01$	$\log N_0 = -4.57 \pm 0.01$
	$\alpha = -0.76 \pm 0.06$	$\alpha = -0.76 \pm 0.05$	$\alpha = -0.76 \pm 0.06$
Thermal SZ effect, simulation	$\log N_0 = -2.36 \pm 0.02$	$\log N_0 = -5.31 \pm 0.02$	$\log N_0 = -2.06 \pm 0.02$
	$\alpha = -1.40 \pm 0.03$	$\alpha = -1.40 \pm 0.06$	$\alpha = -1.40 \pm 0.03$
Kinetic SZ effect, simulation	$\log N_0 = -3.95 \pm 0.01$	$\log N_0 = -3.88 \pm 0.01$	$\log N_0 = -4.02 \pm 0.01$
	$\alpha = -0.72 \pm 0.04$	$\alpha = -0.72 \pm 0.05$	$\alpha = -0.72 \pm 0.05$

6 SUMMARY

All-sky maps for the thermal and kinetic SZ effects are presented, and their characteristics are described in detail. The maps because of their angular resolution and the data storage format chosen (HEALPIX) especially suited for simulations for *Planck*.

(i) The all-sky maps of the thermal and kinetic SZ effects presented here incorporate the correct two-point correlation function, the evolving mass function and the correct size distribution of clusters to within the accuracy of the underlying Hubble-volume simulation and the small-scale adiabatic gas simulations.

(ii) The maps presented here exhibit significant cluster substructure (compare Section 5.1). In spite of this, fits to the Comptonization maps yield angular core radii, the distribution of which is close to the expectation based on the virial theorem (Section 5.2).

(iii) The difference in the distribution of the integrated Comptonizations $\mathcal{Y}$ and $\mathcal{W}$ (Section 5.3) and source counts $N(\langle S \rangle > S_{\rm min})$ (Section 5.6) between values derived from scaling relations compared to those following from template data has been found to be substantial, which hints at possible misestimations of the number of clusters detectable for *Planck*.

(iv) An analytic investigation in Section 4.4 quantified the contribution of the cluster sample to the sky averaged mean thermal Comptonization $\langle y \rangle$ and its variance σ_y. It was found that the clusters within the boundaries in mass ($M > 5 \times 10^{13}\,{\rm M}_{\odot}\,{\rm h}^{-1}$) and redshift ($z < 1.48$) make up $\simeq 40$ per cent of the mean Comptonization, but account for $\sim$98 per cent of the variance. The value for the mean Comptonization corresponds well to that obtained by other authors (Section 5.4).}

(v) The power spectra (Section 5.5) are compatible in amplitude and slope to the ones found by White et al. (2002). On large angular scales, i.e. at small multipole ℓ, deviations from the Poissonianity in the slope of the power spectrum have been found.

(vi) The velocities of the kinetic SZ map correspond to the actual cosmological density environment, i.e. correlated infall velocities are observed due to the formation of superclusters, which highlights a significant improvement in comparison to methods that draw a cluster peculiar velocity from a (Gaussian) distribution and enables searches for the kinetic SZ effect by considering spatial correlations with the thermal SZ effect. The cross-correlation of the thermal with the kinetic SZ map yields a spectrum similar in shape at intermediate amplitudes (see Section 5.5).

Despite the high level of authenticity that the all-sky SZ maps exhibit, there are quite a few issues not being taken account of. The baryon distribution and temperature inside the ICM are governed by processes beyond adiabatic gas physics, for example, in the form of supernova feedback and radiative cooling. Especially, the latter process gives rise to cool cores which may enhance the thermal SZ signal. The ionization inside the clusters was assumed to be complete. Furthermore, the maps contain only collapsed objects, and hence filamentary structures or diffuse gas is not included. Concerning the thermal history of the ICM, reionization had to be neglected. The kinetic map has been constructed without taking into account the velocity fluctuations inside the cluster. This does not pose a problem for *Planck*, but needs to be remedied in high-resolution SZ surveys to be undertaken with the *Atacama Cosmology Telescope* and the *South Pole Telescope*. Yet another imperfection is the lack of non-thermal particle populations that cause the relativistic SZ effect (Enßlin & Kaiser 2000), whose detectability with *Planck* is still a matter of debate.

ACKNOWLEDGMENTS

The authors would like to thank Simon D.M. White for useful comments. Furthermore, we would like to thank the anonymous referee for valuable suggestions.

REFERENCES

Aghanim N., de Luca A., Bouchet F. R., Gispert R., Puget J. L., 1997, A&A, 325, 9
Arnaud M., Evrard A. E., 1999, MNRAS, 305, 631
Bartelmann M., 2001, A&A, 370, 754
Birkinshaw M., 1999, Phys. Rep., 310, 98
Bouchet F. R., Gispert R., 1999, New Astron., 4, 443
Carlstrom J. E., Holder G. P., Reese E. D., 2002, ARA&A, 40, 643
Cavaliere A., Fusco-Femiano R., 1978, A&A, 70, 677
Colberg J. M. et al. (The Virgo Consortium), 2000, MNRAS, 319, 209
da Silva A. C., Kay S. T., Liddle A. R., Thomas P. A., Pearce F. R., Barbosa D., 2001, ApJ, 561, L15
Delabrouille J., Melin J.-B., Bartlett J. G., 2002, ASP Conf. Ser. Vol. 257. AMiBA 2001: High-Z Clusters, Missing Baryons, and CMB Polarization Simulations of Sunyaev–Zel'dovich Maps and Their Applications. Astron. Soc. Pac., San Francisco, p. 81
Dolag K., Hansen F. K., Roncarelli M., Moscardini L., 2005, MNRAS, 363, 29
Eke V. R., Cole S., Frenk C. S., 1996, MNRAS, 282, 263
Enßlin T. A., Kaiser C. R., 2000, A&A, 360, 417
Evrard A. E. et al., 2002, ApJ, 573, 7
Geisbüsch J., Kneissl R., Hobson M., 2005, MNRAS, 360, 41
Górski K. M., Hivon E., Banday A. J., Wandelt B. D., Hansen F. K., Reinecke M., Bartelmann M., 2005, ApJ, 622, 759

Hernandez-Monteagudo C., Verde L., Jimenez R., Spergel D. N., 2006, ApJ, 643, 598
Herranz D., Sanz J. L., Barreiro R. B., López-Caniego M., 2005, MNRAS, 356, 944
Herranz D., Sanz J. L., Hobson M. P., Barreiro R. B., Diego J. M., Martínez-González E., Lasenby A. N., 2002, MNRAS, 336, 1057
Hobson M. P., McLachlan C., 2003, MNRAS, 338, 765
Holder G. P., 2004, ApJ, 602, 18
Jenkins A., Frenk C. S., White S. D. M., Colberg J. M., Cole S., Evrard A. E., Couchman H. M. P., Yoshida N., 2001, MNRAS, 321, 372
Kay S. T., Liddle A. R., Thomas P. A., 2001, MNRAS, 325, 835
Komatsu E., Seljak U., 2002, MNRAS, 336, 1256
Lloyd-Davies E. J., Ponman T. J., Cannon D. B., 2000, MNRAS, 315, 689
Ma C., Fry J. N., 2002, Phys. Rev. Lett., 88, 211301
Mandolesi N. et al., 1995, Planet. Space Sci., 43, 1459
Mathiesen B. F., Evrard A. E., 2001, ApJ, 546, 100
Mohr J. J., Mathiesen B., Evrard A. E., 1999, ApJ, 517, 627
Monaghan J. J., Lattanzio J. C., 1985, A&A, 149, 135
Moscardini L., Bartelmann M., Matarrese S., Andreani P., 2002, MNRAS, 335, 984
Myers A. D., Shanks T., Outram P. J., Frith W. J., Wolfendale A. W., 2004, MNRAS, 347, L67
Nagai D., Kravtsov A. V., Kosowsky A., 2003, ApJ, 587, 524
Navarro J. F., Frenk C. S., White S. D. M., 1995, MNRAS, 275, 720
Persi F. M., Spergel D. N., Cen R., Ostriker J. P., 1995, ApJ, 442, 1
Press W. H., Schechter P., 1974, ApJ, 187, 425
Refregier A., Komatsu E., Spergel D. N., Pen U., 2000, Phys. Rev. D, 61, 123001
Rephaeli Y., 1995, ARA&A, 33, 541
Scaramella R., Cen R., Ostriker J. P., 1993, ApJ, 416, 399
Seljak U., Burwell J., Pen U., 2001, Phys. Rev. D, 63, 063001
Sheth R. K., Tormen G., 1999, MNRAS, 308, 119
Spergel D. N. et al., 2003, ApJS, 148, 175
Springel V., Hernquist L., 2002, MNRAS, 333, 649
Springel V., White M., Hernquist L., 2001, ApJ, 549, 681
Springel V., Yoshida N., White S. D. M., 2001, New Astron., 6, 79
Stöhr F., 1999, High Resolution Simulations of Underdense Regions, Diploma thesis, Munich Technical University
Sunyaev R. A., Zel'dovich I. B., 1972, Comments Astrophys. Space Phys., 4, 173
Sunyaev R. A., Zel'dovich I. B., 1980, ARA&A, 18, 537
Tauber J. A., 2001, in Harwit M., Hauser G., eds, Proc. IAU Symp. 204, The Extragalactic Infrared Background and its Cosmological Implications. Astron. Soc. Pac., San Francisco, p. 493
White M., 2003, ApJ, 597, 650
White M., Hernquist L., Springel V., 2002, ApJ, 579, 16
Wright E. L., 1979, ApJ, 232, 348

This paper has been typeset from a TEX/LATEX file prepared by the author.